Title
Durability of Pt-Alloy Catalyst for Heavy-Duty Polymer Electrolyte Fuel Cell Applications under Realistic Conditions

Journal
ChemElectroChem, 12(8)

ISSN
2196-0216

Authors
Chen, Celine H
Coats, Matthew
Chabot, Florian
et al.

Publication Date
2025-04-14

DOI
10.1002/celc.202400643

ChemElectroChem

Research Article
doi.org/10.1002/celc.202400643

Chemistry Europe
European Chemical Societies Publishing

www.chemelectrochem.org

Durability of Pt-Alloy Catalyst for Heavy-Duty Polymer Electrolyte Fuel Cell Applications under Realistic Conditions

Celine H. Chen,[a, b] Matthew Coats,[c] Florian Chabot,[a, b, d] Yu Morimoto,[b] Plamen Atanassov,[a] Nobumichi Tamura,[d] Jonathan Braaten,[e] Björn M. Stühmeier,[e] Christina Johnston,[e] Svitlana Pylypenko,*[c] Lei Cheng,*[e] and Iryna V. Zenyuk*[a, b]

As an emerging technology, polymer electrolyte fuel cells (PEFCs) powered by clean hydrogen can be a great source of renewable power generation with flexible utilization because of high gravimetric energy density of hydrogen. To be used in real-life applications, PEFCs need to maintain their performance for long-term use under a wide range of conditions. Therefore, it's important to understand the degradation of the PEFC under protocols that are closely related to the catalyst lifetime. Alloying Pt with transitional metal improves catalyst activity. It is also crucial to understand Pt alloys degradation mechanisms to improve their durability. To study durability of Pt alloys, accelerated stress tests (ASTs) are performed on Pt–Co catalyst supported on two types of carbon. Two different AST protocols were being studied: Membrane Electrolyte Assembly (MEA) AST based on the protocol introduced by the Million Mile Fuel Cell Truck consortium in 2023 and Catalyst AST, adopted from the U.S. Department of Energy (DoE).

Introduction

There are growing concerns about energy and environmental challenges due to the consumption of fossil fuels and production of greenhouse gases. As the need for more flexible utilization of renewable energy sources increases, governments and industries across the world are implementing the use of clean hydrogen and target difficult to decarbonize sectors such as heavy-duty transportation, aviation, and shipping due to high gravimetric energy density of hydrogen.[1] In particular, the transportation sector accounts for 26% of U.S. Greenhouse Gas Emissions by in 2020.[2] Light and heavy-duty vehicles (HDVs) account for 83% of the total emissions from the transportation sector.[3] Only 7% of the total vehicles on-road are HDVs but account for 26% of the CO_2 emission in the transportation sector.[2] Annual freight truck miles travelled is projected to increase by 54% by 2050.[2,4,5] Polymer electrolyte fuel cells (PEFCs) have high power density, zero point-of-use emission, and no evident electrolyte decomposition. They have demonstrated great potential in passenger light-duty vehicles (LDVs)[6]; however, their applications in HDVs have attracted attention due to their unique ability to scale driving range at a much smaller additional weight penalty compared to batteries.

Despite the potential of PEFCs for large-scale adoption, initial system cost and durability remain significant challenges. These issues are primarily due to the use of platinum-group metal (PGM) electrocatalysts. In PEFCs, the electrode structure typically consists of platinum nanoparticles dispersed on a carbon support, partially covered by a polymer electrolyte. Platinum is essential for promoting oxygen reduction reaction (ORR), but its high cost makes large-scale adoption economically challenging.[7] Durability is a major challenge and understanding the electrocatalyst degradation and the correlation between physical property changes, such as decrease of electrochemical surface area (ECSA) by Pt dissolution, and performance decay shown in polarization curves, is a top priority.

The largest overpotential in PEFC is caused by ORR in the cathode electrode, and it is comprised of both sluggish kinetics and low oxygen concentrations at the surface of the Pt catalyst. Pt dissolution rates are different for Pt in contact with ionomer and Pt in contact with water (i.e. Pt in the pores).[8] Pt in contact with water can have higher dissolution rates, potentially due to higher Pt ions transport in water environment, without constrains of ionomer. However, the dissolution effects of Pt in pores vs. on the surface of the carbon support have not been well explored.[9,10]

[a] C. H. Chen, F. Chabot, P. Atanassov, I. V. Zenyuk
Department of Chemical & Biomolecular Engineering, University of California Irvine, Irvine, CA, USA
E-mail: Iryna.Zenyuk@uci.edu

[b] C. H. Chen, F. Chabot, Y. Morimoto, I. V. Zenyuk
National Fuel Cell Research Center, University of California Irvine, Irvine, CA, USA

[c] M. Coats, S. Pylypenko
Department of Chemistry, Colorado School of Mines, Golden, CO, USA
E-mail: spylypen@mines.edu

[d] F. Chabot, N. Tamura
Advanced Light Source, Lawrence Berkeley National Laboratory, CA, USA

[e] J. Braaten, B. M. Stühmeier, C. Johnston, L. Cheng
Bosch Research and Technology Center North America, Sunnyvale, CA, USA
E-mail: Lei.Cheng2@us.bosch.com

Supporting information for this article is available on the WWW under https://doi.org/10.1002/celc.202400643

Accelerated Stress Tests (ASTs) and Pt Degradation Mechanism

Repeated oxidation-reduction of Pt nanoparticles during HDV lifetime causes Pt dissolution in the cathode catalyst layer and decrease in the ECSA. Pt ions can migrate in the membrane towards the anode and get reduced by the hydrogen permeation flow inside the membrane, creating a platinum band, or redeposit on larger Pt atoms causing significant particle size growth, via the Ostwald ripening process.[11] Other forms of Pt degradation include agglomeration, collision and coalescence of Pt particles due to migration, Pt particle detachment, and Pt band formation in the membrane due to Pt ions being reduced by cross-over hydrogen.[12]

To simulate operating conditions of heavy-duty drive cycles, ASTs with square waves are performed. The Pt degradation reaction mechanisms during AST cycles was proposed by Khedekar et al[13], where at the beginning of life (BoL), at low potentials only metallic Pt surface is present. During the anodic scan from LPL of 0.6 V to UPL of 0.95 V, Pt dissolution at first occurs at slow rates. However, the OH groups will adsorb on the Pt surface at the potential of 0.8 V and form PtOH and PtO at UPL. During the upper potential hold, Pt dissolution happens at a slow rate. Pt and O exchange the position, in so-called "place-exchange mechanism" and the amount of PtO coverage increases. Degradation during the AST depends on the UPL because at lower UPLs PtO coverage will be lower, having less formation of Pt ions. During the cathodic scan from UPL of 0.95 V to 0.6 V, PtO will be reduced. Ostwald ripening will be the primary cause of ECSA loss and Pt particle size growth.

Use of Pt-Co Catalyst and Effects Co Leaching on Durability

Pt–Co catalyst has better ORR activity compared to Pt.[14] The alloy catalyst can enhance PEFC performance and reduce cost. Alloying elements can weaken the binding strength of oxygenated intermediates on the catalyst surface and facilitate dissociation of oxygen molecules.[15] They also have a lower activation energy, which can lead to a higher power density and a decrease in the number of cells in a stack system and the overall system cost. In particular, Pt_3Co had the optimal binding energy to achieve the maximum ORR activity among the various Pt–Co catalysts.[16]

Although Pt–Co catalyst has better kinetics than pure Pt catalyst, Co leaching can negatively impact the durability. Pt–Co catalyst tends to have a core-shell structure, with Pt as the shell and Pt–Co as the core; Pt dissolution during PEFC operation can cause Co to be exposed, leading to Co leaching.[17,18] Based on the Pourbaix diagram of Co[19], cobalt is in the form of Co^{2+} cation at the PEFC operation range of pH 0–2 and potential of 0–0.9 V. Co^{2+} can be transported through the MEA in two different mechanisms: diffusion, which is driven by water and cation concentration difference, and migration, which is driven by potential gradient. Oxygen tends to diffuse through hydrophilic domains instead of the hydrophobic domains in Nafion withing the catalyst layer, as the oxygen diffusivity in water is four times higher than in Nafion.[20] The decrease in performance of PEFC can be caused by transport limitations as oxygen gas needs to be transported through all of the layers to reach Pt catalyst. However, oxygen transport resistance impedes the flow of oxygen into the cell, causing the concentration of oxygen to be low at the cathode. Oxygen permeation through the ionomer film is especially a major source of transport resistance through the cathode catalyst layer. Co cation contamination in the ionomer can impede oxygen transport because it can decrease oxygen permeation[21] and change the water uptake in the ionomer, affecting both oxygen diffusion in the ionomer films and their adsorption. Co cations leached from Pt–Co catalysts will interact with two SO_3^- side chains, causing crosslinking in the ionomer structure and increasing the enhanced chain stiffness.[22] This phenomenon not only change the structure of the ionomer, reducing its conductivity,[15] but also block the oxygen transport pathway in the ionomer as oxygen cannot be transported to the catalytic sites. As a result, Co leaching can affect the mass activity, protonic resistance, and oxygen transport resistance in the system.

In this study, MEAs with Pt–Co catalysts supported on Vulcan (Vu) and high surface area carbon (HSC) were subjected to two different ASTs protocols. The MEA AST is based on the protocol introduced by the Million Mile Fuel Cell Truck consortium in 2023 and the Catalyst AST is adopted from the DoE catalyst AST protocol. Both AST protocol are conducted in air, having advantages that they can simulate real-world operation of PEFC. The MEA AST had longer dwell time at the potential limits, allowing water equilibrium to be achieved. However, this protocol introduces stressors for both the catalysts and membrane due to operation in dry condition. Performance degradation due to ASTs was studied using electrochemical techniques, including polarization curves and catalyst activity measurements. This study shows that Pt_xCo/HSC has higher degree of polarization loss compared to Pt_xCo/Vu, especially during the MEA AST protocol because of higher degree of particle size growth and Co leaching. The Co leaching was identified through increase in high-frequency resistance (HFR) and proton transport resistance in the catalyst layer. These findings were further confirmed through transmission electron microscopy and energy dispersive x-ray spectroscopy analysis (TEM-EDS). We also observed that the MEA AST protocol was more detrimental to the catalyst durability than the Catalyst AST.

Methods

Materials and Membrane Electrode Assembly (MEA) Preparation

Two types of MEAs were fabricated: PtCo nanoparticles on Vulcan carbon (Vu) (TEC36 V32, 28.9 wt% Pt, 3.2 wt% Co, Tanaka Kikinzoki Kogyo, Japan) and PtCo nanoparticles on high surface area carbon (HSC) (TEC36E32, 29 wt% Pt, 2.3 wt % Co, Tanaka Kikinzoki Kogyo, Japan). Catalyst inks were prepared by mixing the catalyst with deionized water, 2-propanol (99.5 %) (Millipore Sigma, Massachusetts, United States), and Nafion™ dispersion (D521CS, Chemours, Delaware, United States). Ink of PtCo nanoparticles on Vu had I/C ratio of 0.65, solid content of 6.6 wt%, 2-propanol:water of 1 : 2 w/w. Ink of PtCo nanoparticles on HSC had I/C ratio of 0.9, solid content of 5 wt%, 2-propanol:water of 1 : 1 w/w. The inks were roll milled with ZrO_2 balls for 48 hours and coated on a PTFE substrate (50 μm thick) using a wet film applicator with 200 μm and 300 μm thickness for catalysts with Vu and HSC, respectively, on a tape casting machine. X-ray Fluorescence (XRF) was used to determine the Pt loading of the coated decals, which were in the range of 0.15 ± 0.03 mg cm^{-2}. The anode inks were prepared in a similar manner to the PtCo nanoparticles on Vu, with the only difference being the use of Pt/Vu.

The coated decals of 5 cm^2 were then hot pressed on Nafion™ 211 (25.4 μm) at 150 °C for 7 min with a force of ~0.1 kN cm^{-2}. The MEAs were prepared by sandwiching the CCMs between two Freudenberg H23 C6 gas diffusion layers (GDLs). Four MEAs were prepared for each catalyst -two for each AST protocol. In the following results, error bars indicate the standard deviation between the two measurements.

Testing Hardware

Fuel cell quick connect fixture (qCf) coupled with a cell fixture (cF) from balticFuelCells GmbH (Schwerin, Germany) was used, and flow-field with two turn 5 cm^2 x7 serpentine channel was utilized. The cell compression in this setup is pneumatically controlled, so a pneumatic compression pressure of ~0.9 bar was applied to achieve manufacturer-recommended 1–1.1 MPa pressure on the GDL, which resulted in 20–22 % of GDL compression. Polarization curves were performed using 850e fuel cell test system from Scribner Associates (North Carolina, United States). Cyclic voltammograms (CVs), linear sweep voltammograms (LSVs), electrochemical impedance spectroscopies (EISs), CO stripping, mass activity measurements, and the ASTs were performed using Interface 5000 potentiostat from Gamry Instruments (Pennsylvania, United States).

Electrochemical Characterization and AST

At the beginning of testing, each MEA went through a break-in procedure, which consisted of 80 voltage cycles of 0.8 V, 0.5 V, 0.2 V at 80 °C cell temperature in 100 % RH under atmospheric pressure, with hold time of 30 seconds at each potential step and flow rates of 0.5/1 slpm under hydrogen/air (anode/cathode) environment. After voltage cycling, a recovery step, consisted of voltage hold at 0.2 V for 1 hour at 40 °C in 150 % RH under 150 kPa absolute pressure, was applied to recover reversible losses. The recovery step had flow rates of 0.25/0.15 slpm under in a hydrogen/air (anode/cathode) environment.

Polarization curves in hydrogen/oxygen (anode/cathode) and hydrogen/air (anode/cathode) environments were collected at 80 °C in 100 % RH under 150 kPa absolute pressure with gas flow rates of 1 slpm and 2.5 slpm at anode and cathode, respectively. For oxygen cathode environment, 3-minute holds from 0.75 V to open circuit potential with increments of 25 mV were performed to determine mass activity. 4-minute holds from high current density (2 $A.cm^{-2}$) to low current density (0 $A.cm^{-2}$) were performed for air cathode environment. The data collected during the last minute of the holds was averaged and used to plot polarization curves (air) and Tafel plots (oxygen).

LSVs were collected from 0.05 V to 0.5 V at sweep rate of 1 $mV{\cdot}s^{-1}$. EIS was collected at 0.2 V from 20 kHz to 0.1 Hz with 6 points/decade. Both LSV and EIS were performed in hydrogen/ nitrogen (anode/cathode) environment at 80 °C in 100 % RH under atmospheric pressure conditions with gas flow rates of 1 slpm/1 slpm. CV was collected in hydrogen/nitrogen (anode/cathode) environment at 35 °C in 100 % RH under atmospheric pressure conditions with gas flow rates of 1 slpm/1 slpm and with a potential scan from 0.05 V to 1.0 V at a scan rate of 40 $mV{\cdot}s^{-1}$.

CO stripping at 35 °C in 100 % RH under atmospheric pressure conditions was used to determine the ECSA. 5 % H_2 in N_2 with flow rate of 1 slpm was applied at anode throughout the CO stripping experiment. First, three subsequent cycles of CV with a potential scan from 0.05 V to 1.0 V at a scan rate of 40 $mV{\cdot}s^{-1}$ were collected. CO displacement on the Pt surface was performed by flowing 2 % CO in N_2 with flow rate of 1 slpm in cathode for 5 minutes while applying potential of 0.35 V. Then N_2 with flow rate of 1 slpm was purged in the cathode for 30 minutes to remove any excess CO. Lastly, three subsequent cycles of CV with a potential scan from 0.05 V to 1.0 V at a scan rate of 40 $mV{\cdot}s^{-1}$ were performed for CO stripping. The area between the third scan of the CV taken before CO displacement and first scan of CO stripping is used to calculate the ECSA, assuming a charge of 420 $\mu C\,cm^{-2}$ per CO monolayer for Pt.

Two types of AST were performed: MEA AST and Catalyst AST. The MEA AST was performed at 90 °C cell temperature in 50 % RH under 250 kPa absolute pressure. The MEA AST, based on the protocol proposed by the Million Mile Fuel Cell Truck consortium in 2023, comprised of rectangular potential cycles with lower potential limit of 0.675 V, upper potential

limit of 0.925 V, and a dwell time of 30 seconds at each potential. Gas flow rates of 0.1 slpm and 0.25 slpm were used for anode (hydrogen) and cathode (air), respectively. During the AST, each MEA was characterized after 0, 50, and 100 AST hours, which correspond to 0, 3000, and 6000 AST cycles. The MEA AST was performed up to 100 hours because the losses in mass activity were greater than DoE target of 60%. The Catalyst AST comprised of 0.6 V lower potential limit and 0.9 V of upper potential limit with a dwell time of 3 seconds at each potential. Gas flow rates of 0.2 slpm and 0.2 slpm were used for anode (hydrogen) and cathode (air), respectively. During the AST, each MEA was characterized after 0, 50, 100, and 150 AST hours, which correspond to 0, 30,000, 60,000 and 90,000 AST cycles. The Catalyst AST was performed up to 150 hours to stimulate 25,000 hours of heavy-duty lifetime. Air was chosen as the cathode feed in this study instead of nitrogen because air-based ASTs provide a more realistic and stringent evaluation of the catalyst durability in PEFCs. The dominant degradation mechanisms during AST cycling is Ostwald ripening and particle dissolution, which can attributed to ECSA loss and formation of Pt band. The presence of oxygen, which actively participates in oxidation and dissolution processes of platinum nanoparticles, resulting in a faster loss of active surface area compared to inert environment[23]. Khedekar et al. reported that Pt band formation was observed in nitrogen-fed ASTs but not in air-fed ASTs[13].

X-Ray Fluorescence (XRF)

Ex-situ μ-XRF measurements were performed using the XGT-9000 Horiba XRF microscope to check the Pt loading of the electrodes. X-ray energy of 50 keV, measurement time of 300 seconds, a focus distance of 1 mm, and a 1.2 mm capillary were used. Pt loadings were quantified using a calibration curve generated from 1.2 mm capillary spectra of samples with known Pt loadings.

Laboratory X-Ray Diffraction (XRD)

XRD on the catalyst powders were performed in a Rigaku Ultima III diffractometer with a 1.2 kW Cu Kα radiation source operated at $\lambda = 1.5405$ Å. . Rietveld refinement of the XRD data was carried out using GSAS-II software.[24] Al_2O_3 powder was used to calibrate instrument parameters. Measurements were performed on catalysts powders and on MEA. The MEA was fabricated with cathode electrode only to make sure diffraction patterns results from the cathode only. XRD background was refined solely refined using a Chebyschev function while MEA XRD background was refined using both a Chebyschev function and the XRD profile of a bare N211 Membrane. The initial parameters of the crystalline structure were taken from the lattice structure of Pt_3Co published by S.U. Jen[25] and then refined with GSAS-II.

Synchrotron μ-X-Ray Diffraction (μ-XRD)

Micro X-Ray diffraction was conducted at the beamline 12.3.2 of the ALS. A 10 keV X-ray beam was focused to 2x5 μm^2 area onto the cathodic surface of the MEA. The stage angle was tilted by 20° relatively to the incident beam while the Pilatus detector was positioned in reflective mode to cover the scattering angle range between 28° and 73° (2θ). Instrument calibration was performed using the XRD data of Al_2O_3 powder as a reference. The XRD mapping was performed on half of the MEA surface corresponding to the cathode inlet (Figure S1), with a 1x1 mm step size and a 12 s exposure time. The unspoiled MEA surface was preserved for electron microscopy imaging. 2D Diffraction pattern was converted to XRD profiles using XRDSol software, the upgraded version of XMAS.[26] The same software was used to fit the platinum diffraction peak at $2\theta =$ ° with a Lorentzian curve and to extract the full width at half maximum (FWMH) and to determine the average nanoparticle size using Scherrer's Equation:

$$s = \frac{K\lambda}{FWMH.cos\theta} \quad (1)$$

With s the size and K the shape factor commonly set at 0.9.

Transmission Electron Microscopy (TEM)

Samples for TEM analysis were prepared via an ultramicrotomy. An approximately 2 mm x 6 mm sample was extracted from the active area near the outlet of the MEA. A block was prepared using an Araldite 6005 epoxy kit composed of Araldite 6005 (10.7 g), (DMP-30) 2,4,6-Tris-(dimethylaminomethyl) phenol (0.23 g), and Dodecenyl Succinic Anhydride (DDSA: 7. g). A 68 °C pre-heated oven was used to cure the embedded MEA for 16 hours to form a block. Subsequently, a Leica EM Trim2 was used to trim a square shape around the face of the block. Subsequently, a Leica EM UC7 was utilized to ultramicrotome the block using a Diatome diamond knife to produce nominal 100 nm thick cross-sections. The cross-sectioned samples were collected on top of ultrapure deionized water within the diamond knife assembly by use of a perfect loop. The samples were placed onto SPI 3 mm diameter Cu TEM grids (400 mesh slim bar).

A JEOL NEOARM operated at 200 kV was used in scanning transmission electron microscopy mode (STEM). A spot size of C-6, 70 μm aperture, and camera length of 8 cm were used. Five images were acquired at each of the following three areas of the catalyst layer: the gas diffusion layer -catalyst layer interface (GDL-CL), the middle of the catalyst layer (MID), and the membrane-catalyst layer interface (PEM-CL). The magnification between images was kept consistent of 600 kx. Image acquisition was collected over 16 s using the bright field (BF) and annular dark field (ADF) detectors. Compositional information was provided by energy dispersive X-ray spectroscopy while in STEM mode (STEM/EDS).

Through-plane particle size analysis was manually conducted using ImageJ's freehand tool to measure individual particle areas using the raw BF images. Only particles in which the shape could easily be differentiated were analyzed; this excluded some overlapping particles and most agglomerates. The list of measured nanoparticle areas for each region were imported into MATLAB (2023b) to back calculate the subsequent equivalent diameter (rederivation of the equation of an area of a circle to back calculate the diameter). Histograms were generated using a probability distribution function which were binned to 0.5 nm. The histograms were fit to a lognormal distribution to extract the mean and the standard deviation (square root of the variance as reported by the application). The process was repeated until enough images were utilized to ensure a converged average lognormal fit difference of 0.1 nm. An estimate for particle density can be estimated based on using the total number of particles analyzed in the image divided by the total number of images used in the analysis.

Oxford Instruments AZtec software was utilized for acquiring STEM/EDS maps acquired at the same magnification; postprocessing of the EDS compositional data was also done in the same software. EDS signals overlayed on ADF images were processed using the TruMap feature and a standard linear brightness and contrast correction was applied. Relative F, Co, and Pt concentration in atomic percent were quantified. Elements which were deconvoluted but not quantified were Cu (TEM grid), Cr (inside of the TEM), C, O, and S. Density and thickness corrections were not applied. The average F/Pt, F/Co, and Pt/Co were calculated from the relative concentrations.

Results and Discussion

Characterization of the Catalyst Powder and MEAs at BoL

The lattice parameters of both Pt_xCo/Vu and Pt_xCo/HSC in powder and MEA, shown in Figure 1a, were obtained from Rietveld Refinement of XRD profiles. Pt_xCo/Vu had lattice parameters of 3.79 in powder and 3.82 in MEA, while Pt_xCo/HSC had lattice parameters of 3.83 in powder and 3.87 in MEA. According to the literature, the lattice parameter of pure Pt, Pt_3Co, and PtCo are 3.924,[27] 3.854,[25] and 3.768,[28] respectively. Applying the empirical Vegard's law to the Pt–Co alloy, the greater the lattice parameter, the lower the Co content in the catalyst. The lattice parameter of Pt_xCo/HSC in powder is greater than that of Pt_xCo/Vu—there are more Co content in Pt_xCo/HSC than Pt_xCo/Vu. For both catalysts, there was an increase in lattice parameter from powder to MEA, suggesting that Co leaching took place during MEA fabrication as the Nafion dispersion used in inks have acidic pH values due to the sulfonic acid groups in the polymer structure[29]. As shown in the STEM BF images of the Pt_xCo/Vu and Pt_xCo/HSC catalyst nanoparticles at BoL (Figure 1b-**c**), Pt_xCo/Vu has larger particle size than Pt_xCo/HSC. The average particle sizes are ~5.6 nm and ~4.6 nm for BoL MEAs of Pt_xCo/Vu and Pt_xCo/HSC, respectively. Smaller particles size for Pt_xCo/HSC from the STEM BF images corroborates its higher lattice parameter compared to Pt_xCo/Vu in MEA. Smaller particles will have larger surface to volume ratio, therefore higher content of Pt (which is on the surface). Furthermore, the dispersion of the catalyst on the support is different between the two supports, consistent with other reports.[30] Pt_xCo on the Vulcan support appears to be primarily on the surface of the carbon support (Figure 1b). On the other hand, Pt_xCo on the high surface area carbon support appears to be throughout the carbon support (Figure 1c).

The BoL reproducibility of MEAs made with both catalysts, Pt_xCo/Vu and Pt_xCo/HSC, each consisting of three individual MEAs, was assessed across several critical performance

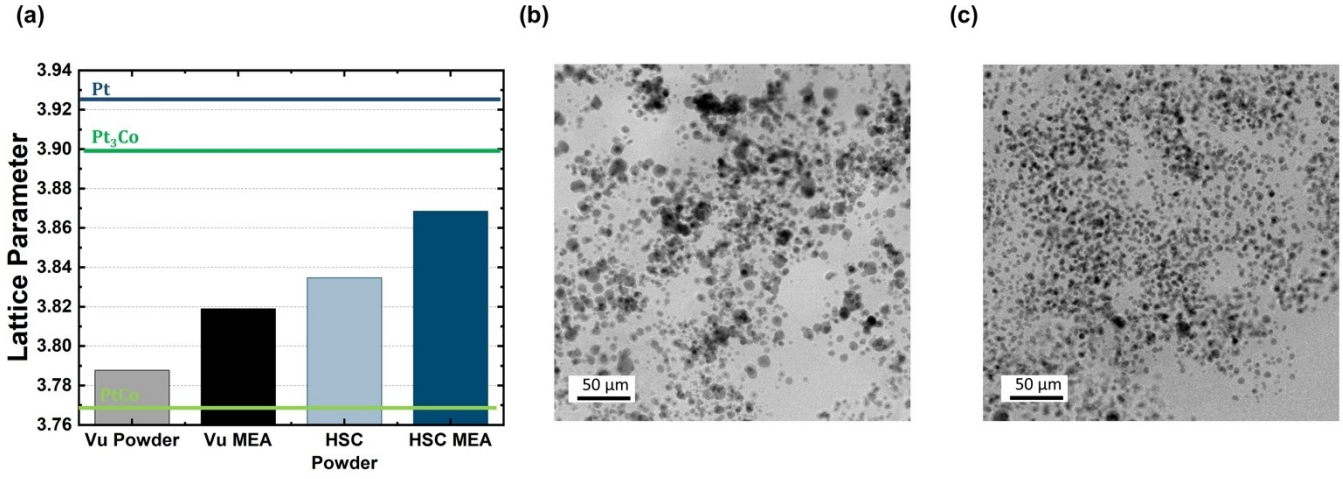

Figure 1. (**a**) Lattice parameter of PtCo/Vu and PtCo/HSC in powder and MEA. (**b**) STEM BF image of the BoL MEA made with Pt_xCo/Vu catalyst (**c**) STEM BF image of the BoL MEA made with Pt_xCo/HSC catalyst.

metrics: polarization curves, HFR, mass activity, and ECSA (Figure S2). The results demonstrate excellent reproducibility for both catalysts, confirming the robustness and consistency of the MEAs prepared with each catalyst type.

Effects of Pt Degradation under MEA AST

Polarization curves with HFR measured at 80°C in 100% RH under 150 kPa of absolute backpressure in H_2-air (anode-cathode) environment for Pt_xCo/Vu and Pt_xCo/HSC during the BoL and after 100 hours of MEA AST were plotted in Figure 2a. Pt_xCo/HSC had better performance at BoL than Pt_xCo/Vu. After 100 hours of MEA AST, increase in kinetic and mass transport cell overpotentials can be observed in both cases; however, Pt_xCo/HSC degraded more than Pt_xCo/Vu, especially in the mass transport region. Overpotential increases of ~34 mV and ~27 mV were seen at current densities of 0.8 A cm^{-2} and 1.5 A cm^{-2}, respectively, for Pt_xCo/Vu. While overpotential increases of ~165 mV and ~302 mV were seen at current densities of 0.8 A cm^{-2} and 1.5 A cm^{-2} for Pt_xCo/HSC. The Pt_xCo/Vu MEA achieved the DoE target of a less than 30 mV[31] increase in overpotential at 1.5 A cm^{-2}.

Figure 2b-**c** show the ECSA, calculated by integrating the CO stripping peak, and the normalized ECSA, which were determined by dividing the ECSA by the initial ECSA value at BoL, plotted at different stages of AST. Pt_xCo/HSC had a ~33% loss in ECSA from 58 m^2 g^{-1} to 39 m^2 g^{-1} at 100 hours of MEA AST, which was greater than the ~14% loss for Pt_xCo/Vu. The ECSA of Pt_xCo/Vu decreased from 38 m^2 g^{-1} to 33 m^2 g^{-1}. Pt_xCo/HSC had smaller catalyst particles at the BoL, and it is expected that smaller particles will become larger through Ostwald ripening mechanism,[32] also resulting in higher surface area loss. At 100 hours of MEA AST, which was established as EoL in this study, both catalysts reached DoE target of less than 40% loss of ECSA. The HFR remained unchanged throughout the AST for Pt_xCo/Vu but increased significantly for Pt_xCo/HSC. Because of the significant increase in HFR for Pt_xCo/HSC, to understand the effect of ECSA loss on performance, the iR-corrected polarization curves were plotted in Figure S3a. After the iR-correction, Pt_xCo/Vu and Pt_xCo/HSC had performance loss of 16 mV and 123 mV at 0.8 A/cm^2, respectively, after 100 hours of MEA AST (Figure S3b). The loss in ECSA agrees well with the observed increase in cell overpotentials.

A 10 mm x18 mm area of each MEA that contains the region with the gas inlet was mapped before and after the MEA AST using micro X-ray diffraction (μ-XRD) to study crystal size of Pt nanoparticles. Figure S1 shows the 10 mm x18 mm area with respect to the 5 cm^2 flow field used. Figure 3a-b and 3d-e show synchrotron μ-XRD maps of the Pt_xCo/Vu and Pt_xCo/HSC MEAs at BoL and after 100 hours of MEA AST, respectively. All four of the maps show homogeneous distribution of crystal sizes through the area of observation and they have also demonstrated unimodal distribution of the catalyst crystal size as shown in Figure 3c and 3f. The crystal size of Pt_xCo/Vu increased from 4.11 nm to

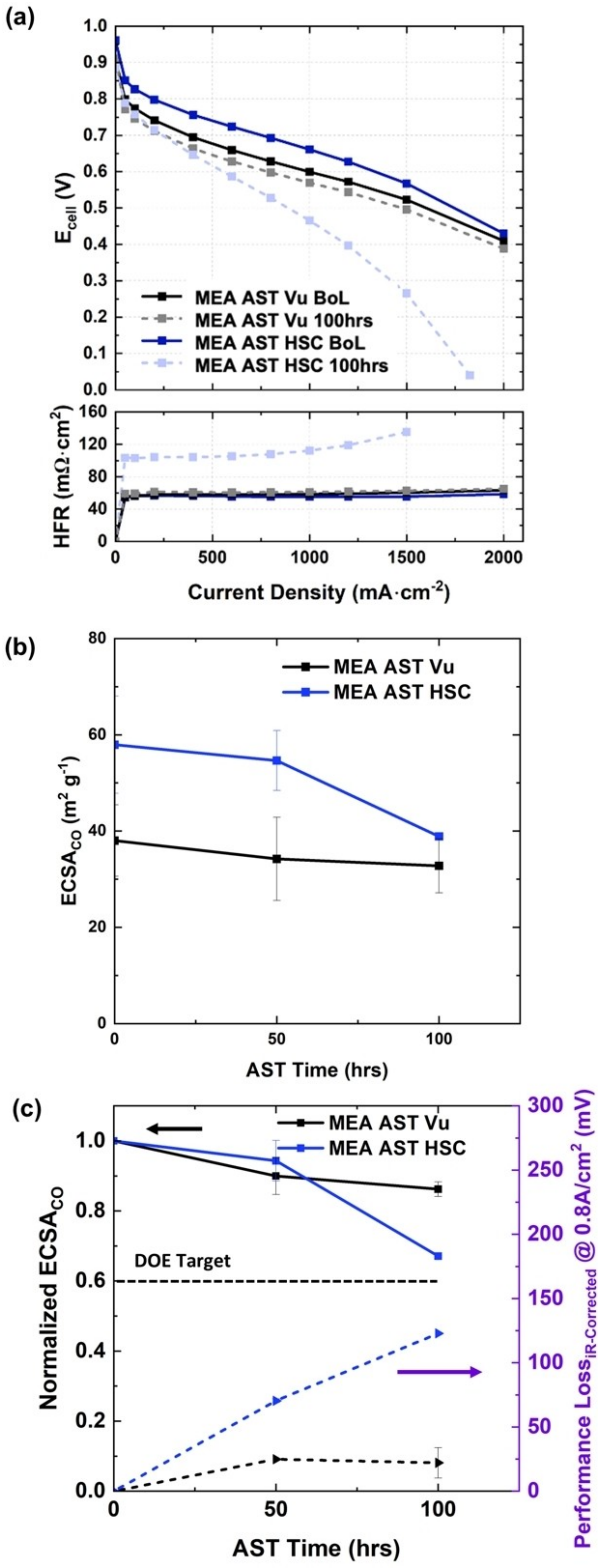

Figure 2. Electrochemical characterization after 0, 50, and 100 hours of MEA AST. (**a**) Polarization curves with HFR collected at 80°C in 100% RH under 150 kPa of absolute backpressure in H_2-air environment. (**b**) ECSA calculated from CO stripping. (**c**) Normalized ECSA calculated from CO stripping and performance loss calculated from polarization curves.

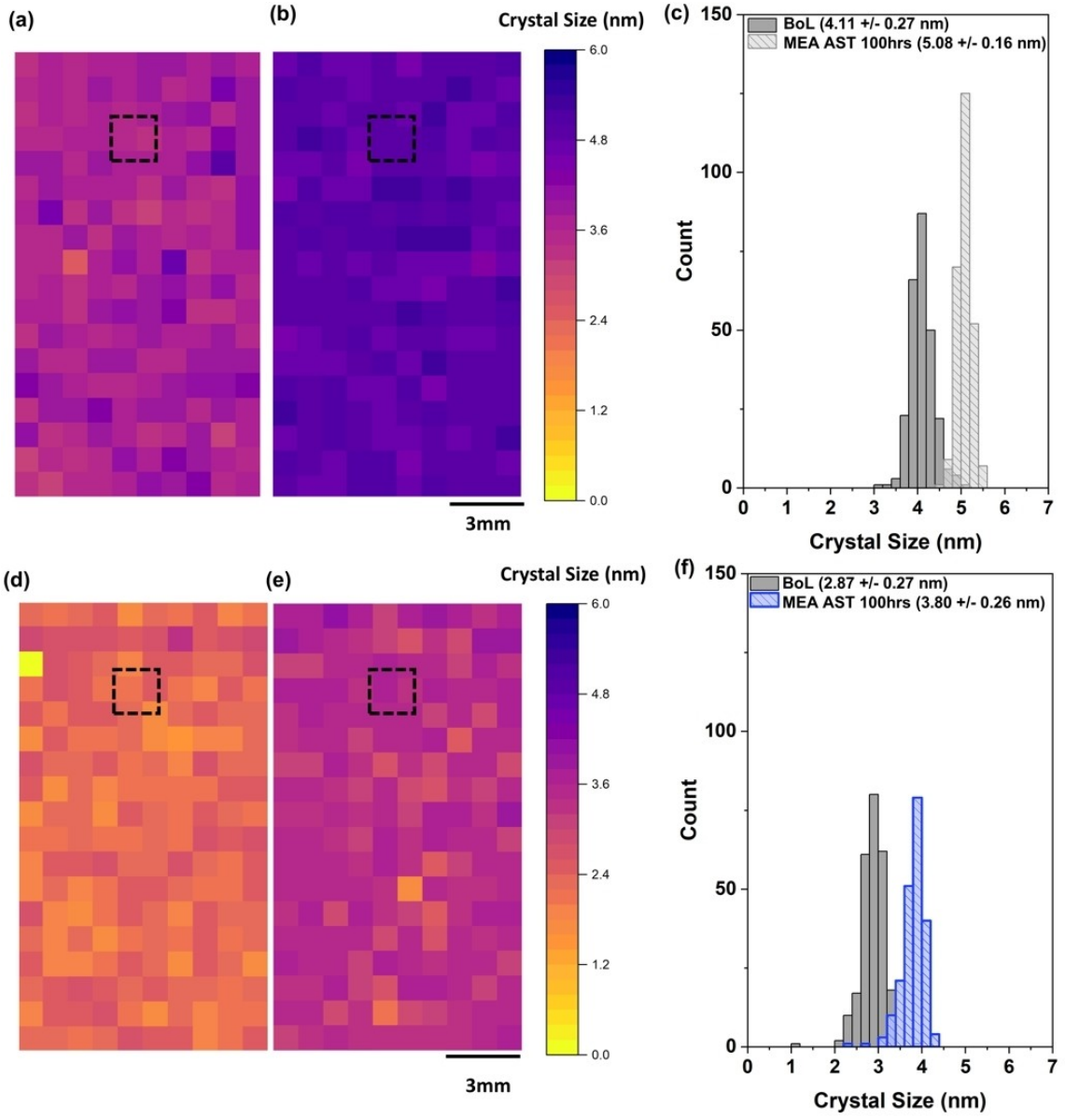

Figure 3. Synchrotron μ-XRD maps of Pt_xCo/Vu (**a**) at BoL, (**b**) after 100 hours of MEA AST, and (**c**) Corresponding crystal size distribution histograms of the μ-XRD maps. Synchrotron μ-XRD maps of Pt_xCo/HSC (**d**) at BoL, (**e**) after 100 hours of MEA AST, and (**f**) Corresponding crystal size distribution histograms of the μ-XRD maps.

5.08 nm, a ~24% increase, while that of Pt_xCo/HSC increased from 2.87 nm to 3.80 nm, a 32% increase. The correlation between increase in crystal size, loss in ECSA, and increase in performance loss can be observed in Figure S3b. Greater increase in crystal size will lead to a greater ECSA and performance loss because repeated oxidation and reduction of Pt during AST can lead to Pt dissolution .[33] Via electrochemical Ostwald ripening, the dominant degradation mechanism, Pt dissolution can lead to decrease in ECSA and increase in crystal size, both of which can result in performance loss.[34,35] Pt_xCo/HSC had greater increase in ECSA loss and crystal size growth than Pt_xCo/Vu because Pt_xCo/HSC had smaller crystal size and particle size than Pt_xCo/Vu at BoL. This suggests that ECSA loss is not as significant in larger particles, as large particles do not grow in size via electrochemical Ostwald ripening as smaller particles because they have smaller surface area to volume ratio.[36]

To corroborate the trends observed with μ-XRD, detailed TEM local imaging with subsequent particle size analysis was conducted across the cathode catalyst layer in the through-plane direction. Unlike μ-XRD which averages all through-plane features (including the membrane and anode) across the in-plane direction, TEM imaging captures local variations within the cathode catalyst layer. Figure 4 demonstrates example BF STEM images of end of life (EoL) MEAs acquired at the GDL-CL, MID, and PEM-CL interfacial regions; furthermore, histograms of particle sizes of BoL and EoL are shown at these three respective regions. The mean particle sizes of

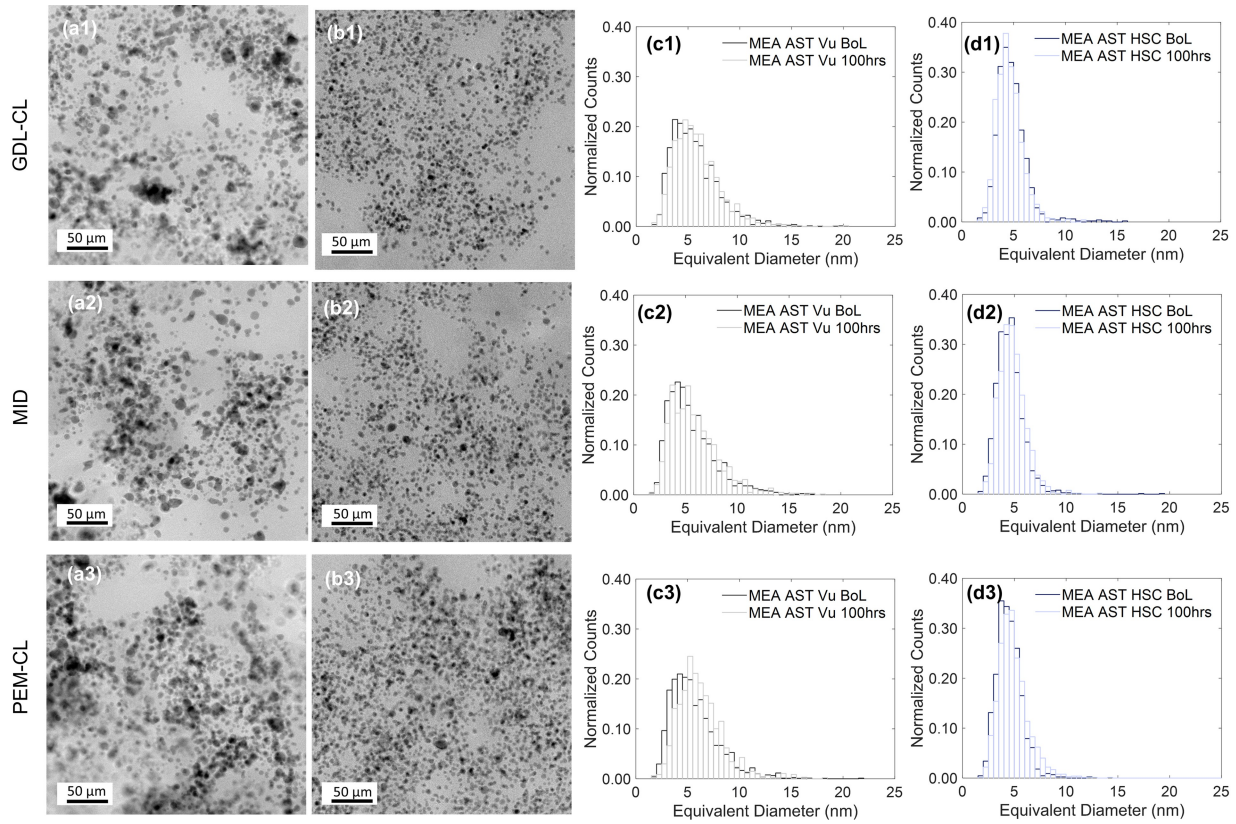

Figure 4. STEM BF images of the (**a**) Pt_xCo/Vu and (**b**) Pt_xCo/HSC MEAs after aging under the MEA AST acquired at the (1) GDL-CL, (2) MID, and (3) PEM-CL. Corresponding histograms of particle sizes measured from localized images in the through-plane direction comparing BoL and after 100 hours of MEA AST are shown in (**c**) and (**d**).

Pt_xCo/Vu increased from ~5.6 nm to ~6.0 nm, with the greatest change at the interface withthe membrane. The relative size in particle size between BoL and EoL increased ~5–10% locally. The Pt_xCo/HSC behaved locally very different compared to Pt_xCo/Vu. At the GDL-CL, the particle size decreased from ~4.8 nm to ~4.6 nm, a ~5% decrease. At the middle of the catalyst layer and at the interface with the membrane, the catalyst slightly increased in size from ~4.6 nm and 4.5 nm to ~4.8 and 4.7 nm, respectively, resulting in an approximately 4% increase. In general, there is a decrease in density of nanoparticles with aging. However, there was no Pt band within the membrane or depletion region in the catalyst layer observed in both EoL MEAs (data not shown). For Pt_xCo/Vu, the measured particle sizes are systematically larger at EoL relative to BoL, especially at the region at the interface with the membrane. On the other hand, the particle density of the EoL Pt_xCo/Vu MEA decreased. For Pt_xCo/HSC, the change in particle size varied spatially in size between BoL and EoL. The density of nanoparticles increased closer towards the interface of the membrane in the catalyst layer and decreased in regions elsewhere in the catalyst layer. Therefore, the mechanism for Pt loss in both MEAs aged under the MEA AST is likely local dissolution and redeposition onto other nanoparticles within the catalyst layer (electrochemical Ostwald ripening) rather than losses to the membrane. The extent of degradation of the nanoparticles can be seen clearly from the bright field images. The Pt_xCo/Vu catalyst having a larger variance in size made aging more susceptible to electrochemical Ostwald ripening while the smaller Pt_xCo/HSC system catalyst being smaller in size made aging more uniform.

Effects of Co Leaching under MEA AST

Decrease in mass activity was observed during the MEA AST, which can be resulting from both ECSA loss and/or Co leaching. At 100 hours of MEA AST, PtC_xo/Vu had ~80% decrease from 0.084 A mg^{-1} to 0.016 A mg^{-1}, while Pt_xCo/HSC at an average of ~66% decrease in mass activity from 0.295 A mg^{-1} to 0.099 A mg^{-1} (Figure 5a-b). Pt_xCo/Vu had a 48% loss in mass activity in the first 50 hours of MEA AST, and Pt_xCo/HSC had a 60% lost in the first 50 hours. Significant decrease of mass activity was observed during the first 50 hours of MEA AST. The ECSA loss during this 50 hours was 10% for Pt_xCo/Vu and 6% for Pt_xCo/HSC which cannot be responsible fully for the dramatic loss in mass activity. Therefore, Co leaching mainly took place during the first 50 hours of AST, especially for Pt_xCo/HSC, which had smaller nanoparticle size and more likely to expose Co to the acidic environment after Pt dissolution. Neither catalyst achieved DoE's target of less than 60% loss in mass activity.

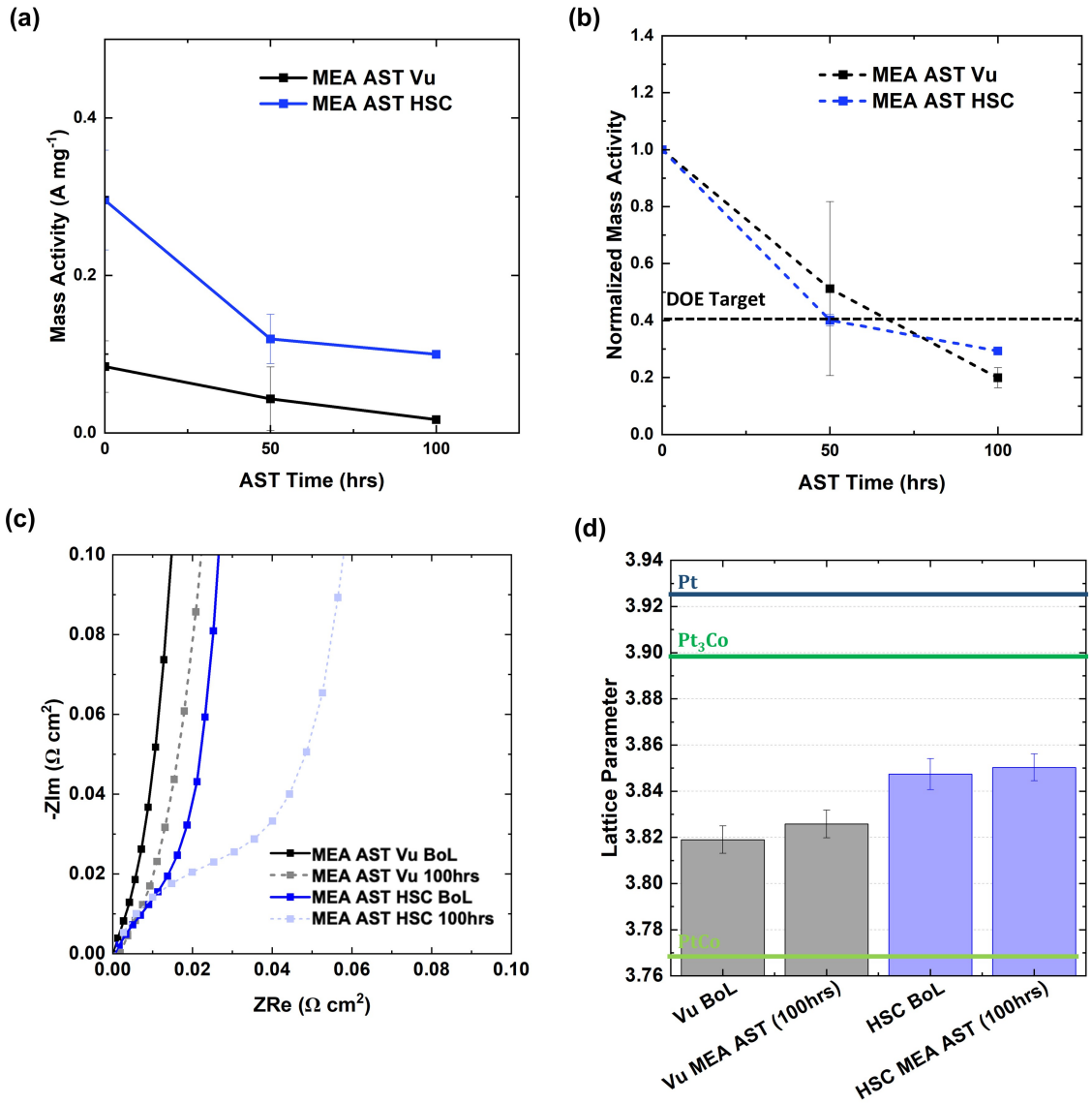

Figure 5. a–c. Electrochemical characterization after 0, 50, and 100 hours of MEA AST. (**a**) Mass activity at 0.9 V calculated from Tafel plots. (**b**) Normalized mass activity at 0.9 V calculated from Tafel plots. (**c**) HFR-corrected Nyquist impedance spectra collected at 80°C in 100% RH under 100 kPa of absolute backpressure in H_2-N_2 environment. (**d**) Lattice parameter calculated from synchrotron μ-XRD.

In the EIS Nyquist plot, protonic resistance, reflected by the 45-degree line, increased for both Pt_xCo/Vu and Pt_xCo/HSC (Figure 5c). However, there was a more significant increase in protonic resistance for Pt_xCo/HSC, confirming Co contamination in the ionomer of cathode catalyst layer[15]. At 100 hours of MEA AST, Pt_xCo/HSC also had a significant increase in HFR (Figure 2a), which can be attributed to Co leaching, diffusion of Co near the membrane, and Co contamination in the membrane[15,37]. Lattice parameter increased slightly for both Pt_xCo/Vu and Pt_xCo/HSC after 100 hours of MEA AST, suggesting loss of Co from the catalysts (Figure 5d). The catalyst with a smaller particle size at the BoL, specifically the Pt_xCo/HSC used in this study, demonstrated higher initial ECSA and mass activity. However, it also underwent greater degradation, ECSA loss, particle size growth, and more Co leaching over time.[38] Catalyst with larger particle size can have better Co retention because larger volume to surface ratio, as Co will mainly reside within the particle, under the Pt skin on the surface of the particle.

The average F/Pt, F/Co, and Pt/Co ratios (Figure 6a, b and c, respectively) are shown for both BoL and MEAs after 100 hrs of MEA AST. It should be emphasized that these are relative and not absolute concentrations. For Pt_xCo/Vu, the F/Pt, F/Co, and Pt/Co decreased in values from BoL to EoL; for Pt_xCo/HSC, the values increased, respectively (Figure 6a-b). In the absence of ionomer heterogeneities, the average F/Pt and F/Co ratios are helpful for determining the relative loss of each metal from the catalyst layer. The average F/Pt ratio should be constant since no Pt is observed as a band in the membrane. The observation of change in F/Pt and F/Co suggests that there are local variations in ionomer content in the catalyst layer and that ionomer concentration is likely

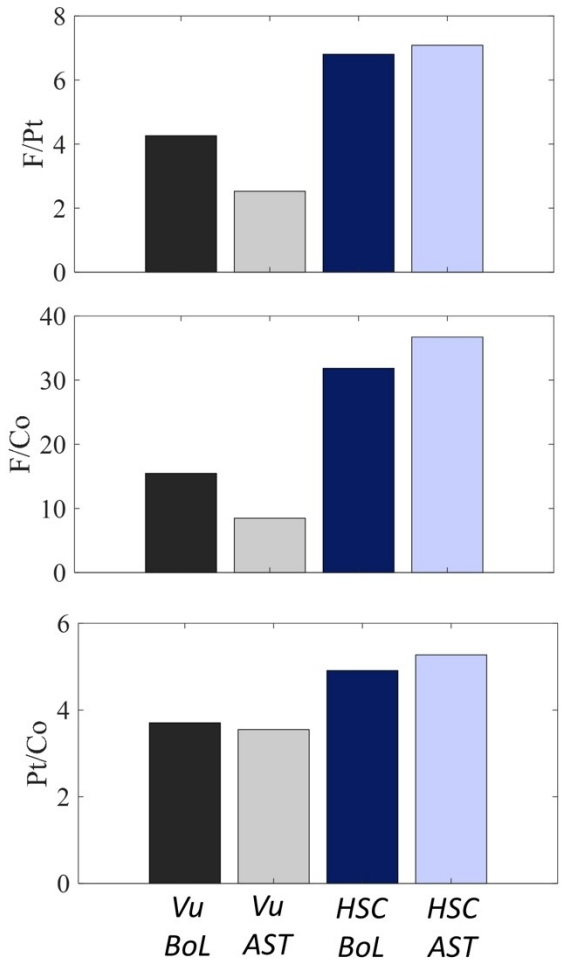

Figure 6. TEM-EDS data showing the average (**a**) F/Pt, (**b**) F/Co, and (**c**) Pt/Co after 0 and 100 hours of MEA AST.

heterogenous (Figure 6a-b). This can likely affect the extent of Co leaching within the catalyst layer. The average Pt/Co ratio at the EoL decreases slightly for Pt_xCo/Vu, but the values are similar to the BoL suggesting that the metals content of the catalyst layer was consistent (Figure 6c). For Pt_xCo/HSC, the increase in the average Pt/Co ratio reveals that the cathode catalyst layer on average becomes Pt richer or Co depleted (Figure 6c). This suggests that the Co had been transported out of the cathode catalyst layer and into areas outside of the cathode catalyst layer. Additional insight into Co leaching can be gained from visual effects of the STEM/EDS maps. Figure S4 STEM HADF overlays of Pt (red) and Co (green) for BoL and EoL within the middle of the cathode catalyst layer. Yellow indicates regions of NPs with a combination of Pt and Co signals. For both BoL MEAs (Figure S4a,c) the difference in initial size appears to dictate the relative signal of Pt and Co, making the Pt_xCo/Vu appear sharper than the Pt_xCo/HSC BoL MEA. The faint green signal surrounding the nanoparticles is being interpreted as Co leached into the ionomer and is more prevalent in the Pt_xCo/HSC BoL MEA compared to the Pt_xCo/Vu BoL MEA (Figure S4a,c). However, the smaller nanoparticle size of Pt_xCo/HSC makes EDS maps of Co and Pt more difficult to interpret compared to the larger nanoparticle size of Pt_xCo/Vu (Figure 4 & Figure S4).

Based on the EIS results, we observed a more significant increase in protonic resistance for Pt_xCo/HSC, confirming that Co leaching from Pt_xCo/HSC was more pronounced, leading to Co contamination in the ionomer of the cathode catalyst layer. However, the changes in the Pt/Co ratio (Figure 6c) before and after the MEA ASTs were not as dramatic as we initially suggested. We believe this discrepancy arises from the differences between electrochemical characterization and TEM-EDS results (Figure 6). Catalyst degradation often occurs non-uniformly across the electrode, and TEM-EDS analyzes localized areas at the nanoscale, which may not fully capture the spatial heterogeneity of the catalyst. In contrast, electrochemical data reflect overall performance changes, primarily influenced by surface activity, while TEM-EDS probes both surface and bulk composition. Additionally, electrochemical characterization is primarily influenced by the small particle size of the catalyst, while TEM imaging captured larger particles that may not contribute significantly to the electrochemical signals.

In addition, although Pt_xCo/HSC exhibited a higher percentage loss in ECSA, it still maintained a higher ECSA compared to the MEA with Pt_xCo/Vu. The increase in HFR and performance loss for Pt_xCo/HSC is likely due to a combination of factors, including not only particle size growth and Co leaching but also other degradation mechanisms such as carbon corrosion, which is more prominent in HSC than in Vu[39]. At electrode potentials of 0.40 - 1.00 V vs. RHE, within which the AST operation range was, the amorphous carbon domains and defective graphite crystallites in the HSC support are preferentially corroded[40]. Carbon oxidation, which initiates near the membrane due to ohmic limitations, can lead to significant structural and performance degradation in the catalyst layer. Carbon oxidation of structural weak points can trigger local electrode collapse, resulting in the formation of an ionomer-dense layer and causing mass transport limitations[41]. This degradation can lead to performance loss. In addition to Co leaching, the observed increase in HFR for Pt_xCo/HSC after 100 hours of MEA AST can also be attributed to carbon corrosion. The HFR increase is likely due to contact loss between the catalyst layer and the GDL[42,43].

Effects of Pt Degradation under Catalyst AST

Catalyst AST was also performed to focus specifically on electrocatalyst degradation. As shown in Figure 7a, polarization curves with HFR measured at 80°C in 100% RH under 150 kPa of absolute backpressure in H_2-air (anode-cathode) environment for Pt_xCo/Vu and Pt_xCo/HSC during BoL and after 150 hours of Catalyst AST were plotted. Pt_xCo/HSC had better performance at BoL than Pt_xCo/Vu, with the exception at 2000 mA cm^{-2}, which can be attributed to transport limitations for high surface area carbon support. After 150 hours of Catalyst AST, increase in kinetic and mass

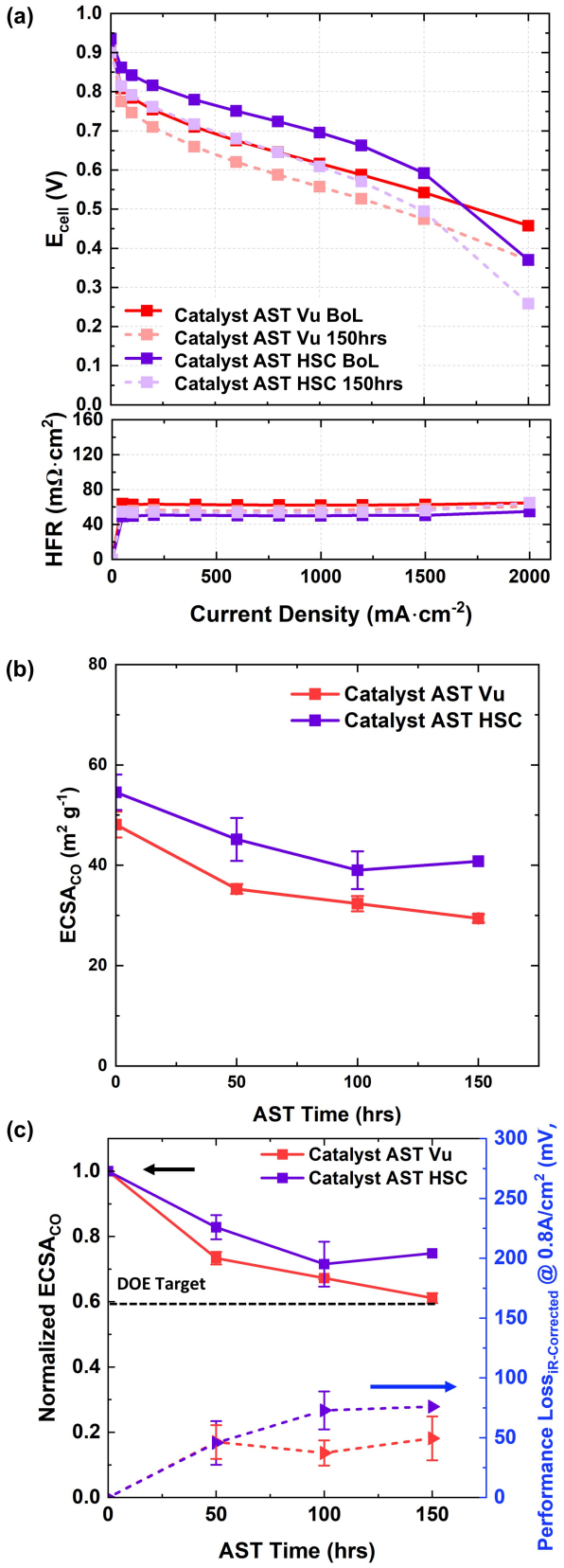

Figure 7. Electrochemical characterization after 0, 50, 100, and 150 hours of Catalyst AST. (**a**) Polarization curves with HFR collected at 80°C in 100% RH under 150 kPa of absolute backpressure in H_2-air environment. (**b**) ECSA calculated from CO stripping. (**c**) Normalized ECSA calculated from CO stripping and performance loss calculated from polarization curves.

transport cell overpotentials can be observed in both cases; however, less degradation was observed in Catalyst AST when compared to MEA AST, especially for Pt_xCo/HSC. Overpotential increases of ~57 mV and ~68 mV were observed at current densities of 0.8 A cm^{-2} and 1.5 A cm^{-2}, respectively, for Pt_xCo/Vu. While overpotential increases of ~79 mV and ~97 mV were observed at current densities of 0.8 A cm^{-2} and 1.5 A cm^{-2} for Pt_xCo/HSC. Neither of the MEAs achieved the DoE target of a less than 30 mV[31] increase in overpotential at 0.8 A cm^{-2} and 1.5 A cm^{-2}.

There is slight reduction in HFR for PtxCo/Vu, which was only observed in the first 50 hours, after which the HFR remained unchanged throughout the rest of the AST (Figure S5a). It has been previously reported and is often attributed to additional cell conditioning[32] and improved contact between the GDL and the catalyst layer, as well as potential changes in the hydration state of the catalyst layer[43]. Over the course of the AST, the catalyst layer may undergo slight structural or morphological adjustments that enhance the contact between the GDL and catalyst, leading to improved electrical conductivity. Additionally, the hydration of the catalyst layer could be optimized during the first few hours of AST, further contributing to a reduction in HFR.

Figure 7b-c show the ECSA and the normalized ECSA plotted at different stages of the Catalyst AST. Pt_xCo/Vu had a ~40% loss in ECSA from 48 m^2 g^{-1} to 29 m^2 g^{-1} at 150 hours of Catalyst AST, which was greater than the ~26% loss for Pt_xCo/HSC. The ECSA of Pt_xCo/HSC decreased from 55 m^2 g^{-1} to 41 m^2 g^{-1}. The iR-corrected polarization curves were plotted in Figure S3c. After the iR-correction, Pt_xCo/Vu and Pt_xCo/HSC had performance loss of 62 mV and 76 mV at 0.8 A/cm^2, respectively, after 150 hours of Catalyst AST (Figure S3d).

Figure 8a-b and 8d-e show synchrotron μ-XRD maps with 10 mm x18 mm in area of the Pt_xCo/Vu and Pt_xCo/HSC MEAs at BoL and after 150 hours of Catalyst AST. All four of the maps demonstrated unimodal distribution of the catalyst crystal size as shown in Figure 8c and 8f. The crystal size of Pt_xCo/Vu increased from 4.11 nm to 4.29 nm, a ~4.4% increase, while that of Pt_xCo/HSC increased from 2.87 nm to 3.82 nm, a 33% increase. The relationship between increase in crystal size, increase in ECSA loss, and increase in performance loss can be observed in Figure S3d. Similar to the results observed between crystal size and performance loss for MEA AST, a clear correlation is observed in Catalyst AST: an increase in crystal size is associated with greater performance loss. However, the correlation between the increase in ECSA loss was not observed in the Catalyst AST, which may be attributed to the fact that, in addition to crystal size growth, other factors could be contributing to the ECSA loss in Pt_xCo/Vu, such as loss of dissolved Pt with water stream.

Effects of Co Leaching under Catalyst AST

Similar to that of MEA AST, significant decrease of mass activity was observed during Catalyst AST and can be

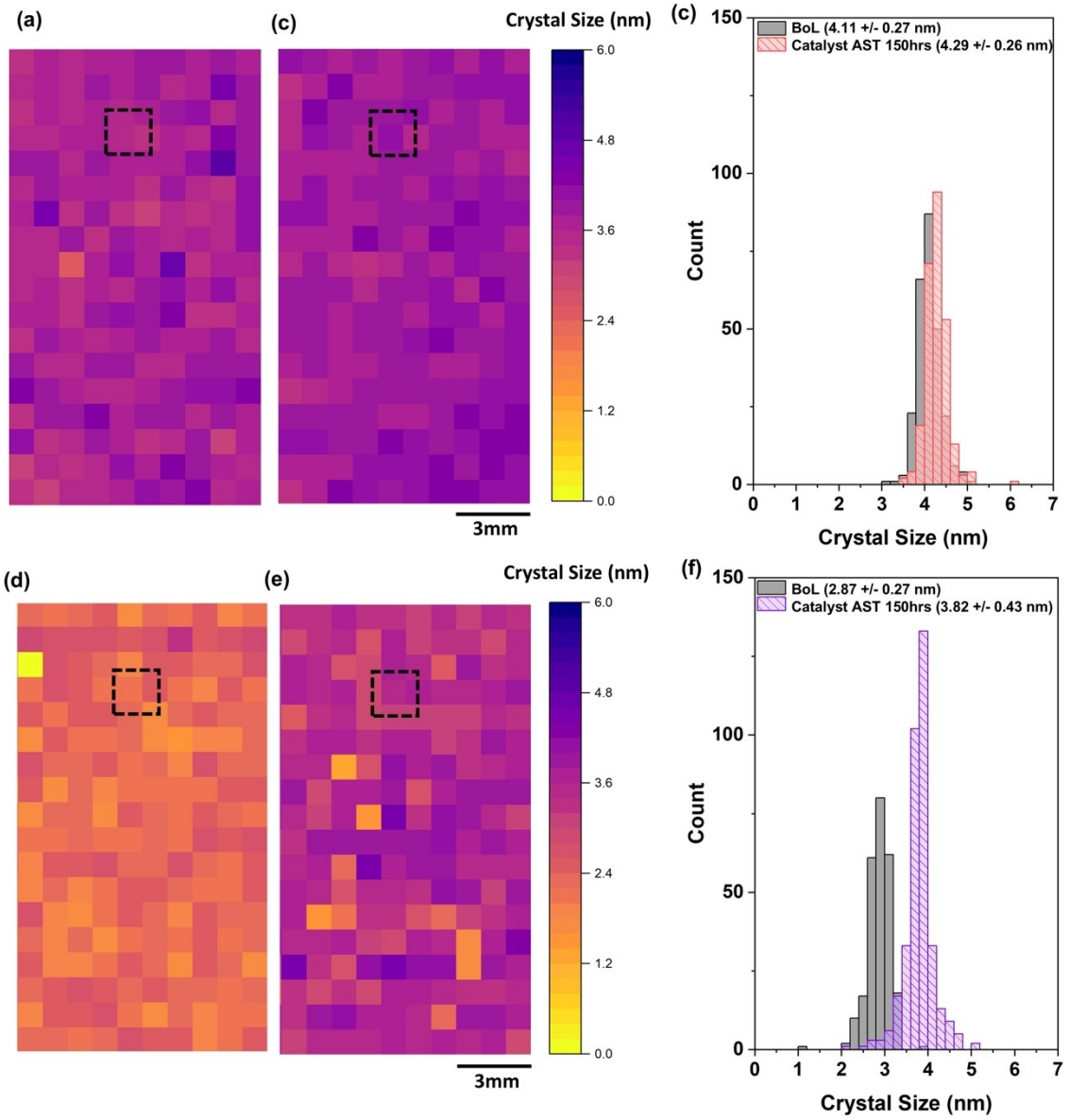

Figure 8. Synchrotron μ-XRD maps of Pt_xCo/Vu (**a**) at BoL, (**b**) after 150 hours of Catalyst AST, and (**c**) Corresponding crystal size distribution histograms of the μ-XRD maps. Synchrotron μ-XRD maps of Pt_xCo/HSC (**d**) at BoL, (**e**) after 150 hours of Catalyst AST, and (**f**) Corresponding crystal size distribution histograms of the μ-XRD maps.

attributed to Co leaching. At 50 hours of Catalyst AST, Pt_xCo/Vu had a 34% loss in mass activity and 27% loss in ECSA, while Pt_xCo/HSC had a 47% loss in mass activity and 17% loss in ECSA. After 150 hours of Catalyst AST, Pt_xCo/Vu had ~31% decrease from 0.098 A mg^{-1} to 0.068 A mg^{-1}, while Pt_xCo/HSC at an average of ~70% decrease in mass activity from 0.39 A mg^{-1} to 0.11 A mg^{-1}(Figure 9a-b). Neither catalyst achieved DoE's target of less than 60% loss in mass activity.

Minimal mass activity was lost between 50 and 150 hours of Catalyst AST for Pt_xCo/Vu. Pt_xCo/HSC had a 47% of the total 70% mass activity lost in the first 50 hours. Similar to the phenomenon observed in MEA AST, Co leaching mainly took place during the first 50 hours of AST, especially for Pt_xCo/HSC, which had smaller nanoparticle size and more likely to expose Co to the acidic environment after Pt dissolution.

In the EIS Nyquist plot, increase in protonic resistance (reflected by the 45-degree line) can be observed for Pt_xCo/HSC. Only a small increase in protonic resistance was observed for Pt_xCo/Vu (Figure 9c), suggesting that Co contamination in the ionomer of cathode catalyst layer was only prominent in the Pt_xCo/HSC[15]. In addition, no significant increase in HFR can be observed in Figure 7a, suggesting that there was no diffusion of Co near the membrane, and Co contamination in the membrane for both catalysts after 150 hours of Catalyst AST.

While the ECSA changes were similar for both Pt_xCo/Vu and Pt_xCo/HSC, more significant loss in mass activity and increase in protonic resistance were observed in the MEA

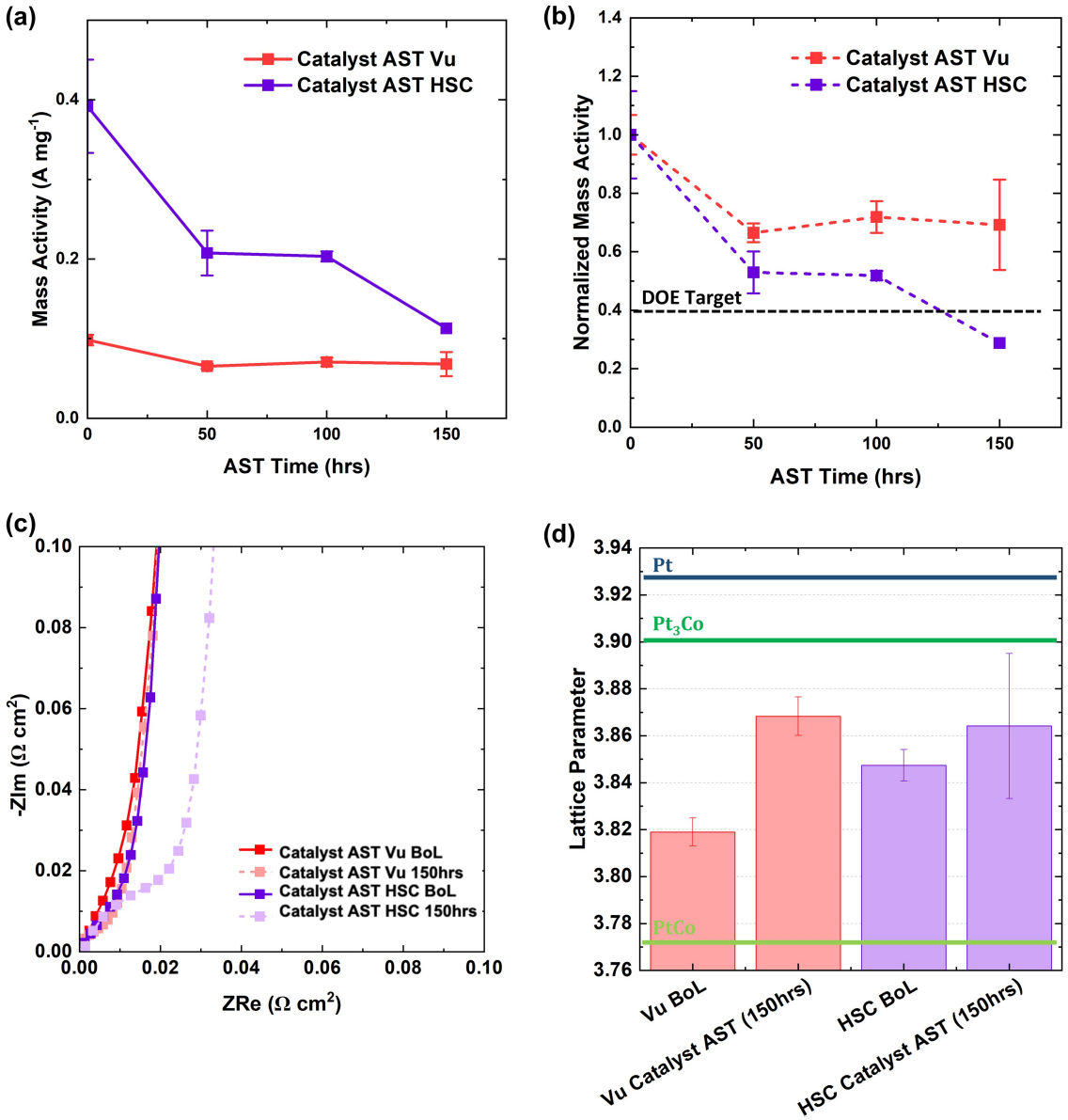

Figure 9. a–c. Electrochemical characterization after 0, 50, 100, and 150 hours of Catalyst AST. (**a**) Mass activity at 0.9 V calculated from Tafel plots. (**b**) Normalized mass activity at 0.9 V calculated from Tafel plots. (**c**) HFR-corrected Nyquist impedance spectra collected at 80°C in 100% RH under 100 kPa of absolute backpressure in H_2-N_2 environment. (**d**) Lattice parameter calculated from synchrotron μ-XRD.

with Pt_xCo/HSC when compared to Pt_xCo/Vu. Lattice parameter increased for both Pt_xCo/Vu and Pt_xCo/HSC at the EoL of Catalyst AST, suggesting loss of Co from the catalysts (Figure 9d). However, the lattice parameter of Pt_xCo/Vu increased more compared that of Pt_xCo/HSC. One possible explanation for this observation is that Co leaching may occur non-uniformly across the catalyst layer. This means that certain areas of the catalyst layer may experience more severe degradation, especially in the case of the smaller particles in Pt_xCo/HSC, which are more prone to Co leaching. However, as the XRD data provides an average structural analysis, it might mask localized changes in the catalyst. The lattice parameter changes observed in Figure 9, where the MEA with Pt_xCo/Vu showed a more pronounced increase in the lattice parameter compared to Pt_xCo/HSC, suggest that Co leaching and structural changes might be more localized or subtle for Pt_xCo/HSC. Furthermore, smaller catalyst particles are more susceptible to Co leaching, but their contribution to the XRD signal could be overshadowed by the larger, more stable particles, which would lead to a less noticeable shift in the lattice parameter at the macro level. This could explain why the changes in mass activity appear more dramatic for Pt_xCo/HSC.

Comparison of AST Protocols

Overall, Pt_xCo/HSC experienced more degradation than Pt_xCo/Vu, and more in MEA AST than Catalyst AST. The higher cell operation temperature, higher upper potential limit and longer hold time of 30s for the MEA AST dictate dissolution of Pt and leaching of Co in Pt_xCo/HSC, which are the main degradation mechanism in heavy-duty vehicles [44–47]. The smaller particle size of Pt_xCo/HSC exacerbated the effects of Pt dissolution and Co leaching the cell performance.[38]

Figure S6 shows measured cell voltages for various geometric current densities (0.4, 0.8, 1.5, and 2.0 A cm^{-2}) as a function of cathode roughness factor (rf), the electrochemically active Pt surface area per geometric electrode area[48], over the course of the two different ASTs. For Pt-alloys, transition metal leaching, as observed in this study has impact on polarization. The measured cell voltages match well between the four samples at low current densities, especially for Pt_xCo/Vu and Pt_xCo/HSC with Catalyst AST, suggesting that the degradation mechanism for both catalysts under Catalyst AST were similar in the kinetic region. At high current densities, there were discrepancies between measured cell voltages – same amount of decrease in rf did not lead to the same amount of decrease in cell voltage. Pt_xCo/HSC with MEA AST at 2.0 A cm^{-2} had the largest loss in cell voltage, suggesting that ECSA loss, which is a reflected by rf values, was not the single cause for loss in polarization. Co leaching also played a significant role.

The degradation mechanism differed significantly for Pt_xCo/Vu and Pt_xCo/HSC. Discrepancy was large in the high current density region between Pt_xCo/Vu and Pt_xCo/HSC as the oxygen transport resistance can be affected by Co leaching. When Co contamination was present in the ionomer of the cathode catalyst layer, crosslinking in the ionomer structure can block the oxygen transport channels in the ionomer, increasing oxygen transport resistance.[22] When Co contamination was present in the membrane, HFR increased and lead to greater ohmic resistance.

50 hours of Catalyst AST reported in our study correspond to 30,000 cycles, which is consistent with the catalyst durability targets for light-duty vehicles. This provides a basis for comparison with previous studies on light-duty vehicles. Increase in kinetic and mass transport cell overpotentials can be observed between BoL and 50 hours of Catalyst AST and 50 hours and 150 hours of Catalyst AST (Figure S5). For Pt_xCo/Vu, overpotential increases of ~30 mV and ~57 mV were observed after 50 hours and 150 hours of AST, respectively, at current densities of 0.8 A cm^{-2}. And overpotential increases of ~34 mV and ~68 mV were observed after 50 hours and 150 hours of AST, respectively, at current densities of 1.5 A cm^{-2} (Figure S5a). For Pt_xCo/HSC, overpotential increases of ~42 mV and ~79 mV were observed after 50 hours and 150 hours of AST, respectively, at current densities of 0.8 A cm^{-2}. And overpotential increases of ~41 mV and ~97 mV were observed after 50 hours and 150 hours of AST, respectively, at current densities of 1.5 A cm^{-2} (Figure S5b).

The data revealed that the overpotential increase in the first 50 hours of AST is relatively similar to the increase observed between 50 and 150 hours of AST for both catalysts. This consistent rate of increase in overpotential during both the first 50 hours and the subsequent 50–150 hours suggests that the degradation process proceeds steadily throughout the entire AST period. And the results for both catalysts with the Catalyst AST in Figure S6 shows relatively linear relationship over the course of AST between cathode rf and cell voltages, except at 2 A cm^{-2}, suggesting Pt degradation mechanism during the first 50 hours (representing light-duty vehicle lifetime) and 50–150 hours (representing the difference between light- and heavy-duty vehicle lifetime) were similar. Rate of degradation was faster during the first 50 hours than during the 50–150 hours of AST. At 2 A cm^{-2} which is dominated by transport overpotentials, the relationship between cathode rf and cell voltages deviates from linearity, suggesting Co leaching were different for light- and heavy-duty lifetime.

Conclusions

In this study, catalyst durability of PEFCs for heavy-duty applications was investigated by performing two different AST protocols: MEA AST, based on the protocol introduced by the Million Mile Fuel Cell Truck consortium in 2023, and Catalyst AST, adopted from the DoE catalyst AST protocol. Pt–Co catalysts, which have the highest activity among all the Pt-alloy catalysts, on two different types of carbon support (Vu and HSC) were studied. For both catalysts, there was an increase in lattice parameter from powder to MEA, suggesting that Co leaching took place during MEA fabrication as the Nafion dispersion used in inks has acidic pH values.

For MEA AST, Pt_xCo/HSC degraded more than Pt_xCo/Vu with a greater increase in crystal size and in performance loss, and greater loss in ECSA and mass activity. Pt_xCo/HAS had smaller catalyst particles at the BoL, which have larger surface to volume ratio. Through Ostwald ripening mechanism smaller particles become larger, resulting in higher ECSA loss. The larger surface to volume ratio in smaller particles also is more likely to expose Co to the acidic environment, causing more Co leaching. More degradation was observed in MEA AST due to its higher cell operation temperature, higher upper potential limit and longer hold time, exacerbated the effects of Pt dissolution and Co leaching the cell performance.

Overall, Pt_xCo/HSC experienced more degradation than Pt_xCo/Vu, and more in MEA AST than Catalyst AST. The main degradation mechanism in heavy-duty fuel cells are Pt dissolution and Co leaching. The smaller particle size of Pt_xCo/HSC exacerbated the effects of Pt dissolution and Co leaching the cell performance.

Comparing the two AST protocols, the MEA AST resulted in more severe degradation than the Catalyst AST. The higher operating temperature, upper potential limit, and longer

dwell time in the MEA AST accelerated Pt dissolution and Co leaching, exacerbating both ohmic and mass transport limitations. These findings highlight the necessity of optimizing catalyst support structures and mitigating Co dissolution to enhance long-term fuel cell performance.

In the Catalyst AST, the first 50 hours represent light-duty vehicle lifetime, and 50–150 hours represent the difference between light- and heavy-duty vehicle lifetime. Pt degradation mechanism was similar for light- and heavy-duty fuel cells, but the rate of degradation was faster during the first 50 hours than during the 50th to 150th hour of AST. However, the degradation mechanism related to Co leaching was different between light- and heavy-duty lifetime.

Overall, this study provides critical insights into the degradation pathways of Pt–Co catalysts in PEFCs, emphasizing the need for durable catalyst designs and improved operational strategies for heavy-duty applications. Future research should focus on developing more stable Pt-alloy catalysts and refining AST protocols to better replicate real-world fuel cell conditions.

Author Contributions

C.C., M.C., and F.C. were chiefly responsible for most of the experiments. F.C. and L.C. performed XRD experiments at the synchrotron. M.C. and S.P. performed microscopy experiments. M.C., F.C., S.P., B.S., J.B., C.J. L.C, Y.M., and I.Z. helped with data interpretation and did conception of the study. C.C. produced the first manuscript draft and all the authors edited it. S.P., L.C., C.J., P.A. and I.Z. obtained funding support and oversaw the study.

Acknowledgements

XRF was performed at HIMaC^2 Analytic Laboratory, a user facility operated by the Horiba Institute for Mobility and Connectivity, University of California, Irvine. The Advanced Light Source is supported by the Director, Office of Science, Office of Basic Energy Sciences, of the U.S. Department of Energy under Contract No. DE-AC02-05CH11231. STEM/EDS analysis was conducted on the JEOL NEOARM AC-STEM at the University of New Mexico's Nanomaterials Characterization Facility which was supported by NSF grant DMR-1829731 and NASA Emerging Worlds grant 80NSSC21K1757. We also thank Emma Carstens for assisting with particle size analysis.

Conflict of Interests

The authors declare no competing interests.

Data Availability Statement

The data that supports the plots within this paper and other findings of this study are available from the corresponding author upon reasonable request.

[1] L. Zhang, C. Jia, F. Bai, W. Wang, S. An, K. Zhao, Z. Li, J. Li, H. Sun, *Fuel* **2024**, *355*. https://doi.org/10.1016/j.fuel.2023.129455.
[2] EPA. Inventory of US Greenhouse Gas Emissions and Sinks, 1990 to 2020. 2022.
[3] Budget Office, C. *Emissions of Carbon Dioxide in the Transportation Sector At a Glance*. www.cbo.gov/publication/58566.
[4] D. Cooke, *Engines for Change From Cell Phones to Sodas, How New Truck Standards Can Improve the Way America Ships Goods*; 2013.
[5] D. A. Cullen, K. C. Neyerlin, R. K. Ahluwalia, R. Mukundan, K. L. More, R. L. Borup, A. Z. Weber, D. J. Myers, A. Kusoglu, *Nat Energy* **2021**, *6* (5), 462–474. https://doi.org/10.1038/s41560-021-00775-z.
[6] T. M. Testing, *Toyota Mirai Testing; DOE Hydrogen and Fuel Cells Program FY 2018 Annual Progress Report*; **2018**. https://www.energy.gov/eere/fuelcells/downloads/fuel-cell-technologies-office-multi-year-research-development-and-22.
[7] A. Kampker, P. Ayvaz, C. Schön, J. Karstedt, R. Förstmann, F. Welker, *Int J Hydrogen Energy* **2020**, *45* (53), 29288–29296. https://doi.org/10.1016/j.ijhydene.2020.07.180.
[8] A. Perego, A. Avid, D. N. Mamania, Y. Chen, P. Atanassov, H. Yildirim, M. Odgaard, I. V. Zenyuk, *Appl Catal B* **2022**, *301*. https://doi.org/10.1016/j.apcatb.2021.120810.
[9] V. Yarlagadda, N. Ramaswamy, R. S. Kukreja, S. Kumaraguru, *J Power Sources* **2022**, *532*. https://doi.org/10.1016/j.jpowsour.2022.231349.
[10] S. Cherevko, N. Kulyk, K. J. J. Mayrhofer, *Nano Energy* **2016**, *29*, 275–298. https://doi.org/10.1016/j.nanoen.2016.03.005.
[11] C. H. Chen, K. Khedekar, A. Zaffora, M. Santamaria, M. Coats, S. Pylypenko, P. A. García-Salaberri, J. Braaten, P. Atanassov, N. Tamura, C. Johnston, L. Cheng, I. V. Zenyuk, *ACS Appl Energy Mater* **2024**, *7* (14), 5736–5744. https://doi.org/10.1021/acsaem.4c00803.
[12] N. Hodnik, G. Dehm, K. J. J. Mayrhofer, *Acc Chem Res* **2016**, *49* (9), 2015–2022. https://doi.org/10.1021/acs.accounts.6b00330.
[13] K. Khedekar, M. Rezaei Talarposhti, M. M. Besli, S. Kuppan, A. Perego, Y. Chen, M. Metzger, S. Stewart, P. Atanassov, N. Tamura, N. Craig, L. Cheng, C. M. Johnston, I. V. Zenyuk, *Adv Energy Mater* **2021**, *11* (35). https://doi.org/10.1002/aenm.202101794.
[14] S. Choi Il, S. U. Lee, W. Y. Kim, R. Choi, K. Hong, K. M. Nam, S. W. Han, J. T. Park, *ACS Appl Mater Interfaces* **2012**, *4* (11), 6228–6234. https://doi.org/10.1021/am301824w.
[15] C. H. Lee, X. Wang, J. K. Peng, A. Katzenberg, R. K. Ahluwalia, A. Kusoglu, S. Komini Babu, J. S. Spendelow, R. Mukundan, R. L. Borup, T *ACS Appl Mater Interfaces* **2022**, *14* (31), 35555–35568. https://doi.org/10.1021/acsami.2c07085.
[16] S. Sankarasubramanian, N. Singh, F. Mizuno, J. Prakash, *J Power Sources* **2016**, *319*, 202–209. https://doi.org/10.1016/j.jpowsour.2016.04.054.
[17] P. Weber, D. J. Weber, C. Dosche, M. Oezaslan, *ACS Catal* **2022**, *12* (11), 6394–6408. https://doi.org/10.1021/acscatal.2c00514.
[18] F. Maillard, L. Dubau, J. Durst, M. Chatenet, J. André, E. Rossinot, *Electrochem commun* **2010**, *12* (9), 1161–1164. https://doi.org/10.1016/j.elecom.2010.06.007.
[19] E. M. Garcia, J. S. Santos, E. C. Pereira, M. B. J. G. Freitas, *J Power Sources* **2008**, *185* (1), 549–553. https://doi.org/10.1016/j.jpowsour.2008.07.011.
[20] Q. Zhao, P. Majsztrik, J. Benziger, *Journal of Physical Chemistry B* **2011**, *115* (12), 2717–2727. https://doi.org/10.1021/jp1112125.
[21] J. P. Braaten, X. Xu, Y. Cai, A. Kongkanand, S. Litster, *J Electrochem Soc* **2019**, *166* (16), F1337–F1343. https://doi.org/10.1149/2.0671916jes.
[22] H. Li, J. You, X. Cheng, X. Yan, S. Shen, J. Zhang, *Chemical Engineering Journal* **2023**, *453*. https://doi.org/10.1016/j.cej.2022.139945.
[23] K. Paperzh, A. Alekseenko, I. Pankov, V. Guterman, *Journal of Electroanalytical Chemistry* **2024**, *952*. https://doi.org/10.1016/j.jelechem.2023.117972.
[24] B. H. Toby, R. B. Von Dreele, *J Appl Crystallogr* **2013**, *46* (2), 544–549. https://doi.org/10.1107/S0021889813003531.
[25] S. U. Jen, *AILILO~ AND COMn~DUNDS Effect of Atomic Order on Some Physical Properties of C025Pt75*; 1996; Vol. 234.
[26] N. Tamura, *Strain and Dislocation Gradients from Diffraction: Spatially-Resolved Local Structure and Defects*; Imperial College Press, **2014**; pp 125–155. https://doi.org/10.1142/9781908979636_0004.

[27] J. W. Edwards, R. Speiser, H. L. Johnston, *J Appl Phys* **1951**, *22* (4), 424–428. https://doi.org/10.1063/1.1699977.
[28] J. C. Woollew, J. I. Phii, S. hN, *JOURNAL OF THE LESS-COMMON METALS 461 ORDERING IN CoPt-CrPt AND CoPt-MnPt ALLOYS of Sottr~zglmn (Gwnt Bit&)*.
[29] S. A. Berlinger, B. D. McCloskey, A. Z. Weber, *Journal of Physical Chemistry B* **2018**, *122* (31), 7790–7796. https://doi.org/10.1021/acs.jpcb.8b06493.
[30] E. Padgett, N. Andrejevic, Z. Liu, A. Kongkanand, W. Gu, K. Moriyama, Y. Jiang, S. Kumaraguru, T. E. Moylan, R. Kukreja, D. A. Muller, *J Electrochem Soc* **2018**, *165* (3), F173–F180. https://doi.org/10.1149/2.0541803jes.
[31] DOE Fuel Cell Technologies Office. Electrocatalyst Durability Protocols for PEM Fuel Cells. **2016**, *2015*, 1–58.
[32] K. Khedekar, A. Zaffora, M. Santamaria, M. Coats, S. Pylypenko, J. Braaten, P. Atanassov, N. Tamura, L. Cheng, C. Johnston, I. V. Zenyuk, *Nat Catal* **2023**, *6* (8), 676–686. https://doi.org/10.1038/s41929-023-00993-6.
[33] S. Cherevko, N. Kulyk, K. J. J. Mayrhofer, *Nano Energy* **2016**, *29*, 275–298. https://doi.org/10.1016/j.nanoen.2016.03.005.
[34] R. Borup, J. Meyers, B. Pivovar, Y. S. Kim, R. Mukundan, N. Garland, D. Myers, M. Wilson, F. Garzon, D. Wood, P. Zelenay, K. More, K. Stroh, T. Zawodzinski, J. Boncella, J. E. McGrath, M. Inaba, K. Miyatake, M. Hori, K. Ota, Z. Ogumi, S. Miyata, A. Nishikata, Z. Siroma, Y. Uchimoto, K. Yasuda, K. I. Kimijima, N. Iwashita, *Chemical Reviews.* **2007**, pp 3904–3951. https://doi.org/10.1021/cr050182 l.
[35] R. L. Borup, A. Kusoglu, K. C. Neyerlin, R. Mukundan, R. K. Ahluwalia, D. A. Cullen, K. L. More, A. Z. Weber, D. J. Myers, *Current Opinion in Electrochemistry*. Elsevier B. V. June 1, **2020**, pp 192–200. https://doi.org/10.1016/j.coelec.2020.02.007.
[36] S. Stariha, N. Macauley, B. T. Sneed, D. Langlois, K. L. More, R. Mukundan, R. L. Borup, *J Electrochem Soc* **2018**, *165* (7), F492–F501. https://doi.org/10.1149/2.0881807jes.
[37] M. A. Schilling, T. Lazaridis, V. Meier, M. Hanauer, H. A. Gasteiger, *J Electrochem Soc* **2025**, *172* (1), 014501. https://doi.org/10.1149/1945-7111/ada188.
[38] M. Gummalla, S. C. Ball, D. A. Condit, S. Rasouli, K. Yu, P. J. Ferreira, D. J. Myers, Z. Yang, *Catalysts* **2015**, *5* (2), 926–948. https://doi.org/10.3390/catal5020926.
[39] N. Macauley, D. D. Papadias, J. Fairweather, D. Spernjak, D. Langlois, R. Ahluwalia, K. L. More, R. Mukundan, R. L. Borup, *J Electrochem Soc* **2018**, *165* (6), F3148–F3160. https://doi.org/10.1149/2.0061806jes.
[40] L. Castanheira, L. Dubau, M. Mermoux, G. Berthomé, N. Caqué, E. Rossinot, M. Chatenet, F. Maillard, *ACS Catal* **2014**, *4* (7), 2258–2267. https://doi.org/10.1021/cs500449q.
[41] L. Strandberg, V. Shokhen, M. Skoglundh, B. Wickman, *ACS Catalysis* **2024**, *14* (11), 8494–8504. https://doi.org/10.1021/acscatal.4c00417.
[42] P. Saha, K. Khedekar, H. Wang, P. Atanassov, L. Cheng, S. Stewart, C. Johnston, I. V. Zenyuk, *J Mater Chem A Mater* **2022**, *10* (23), 12551–12562. https://doi.org/10.1039/d2ta02666j.
[43] Y. Qi, Y. Huang, Z. Gao, C. H. Chen, A. Perego, H. Yildirim, M. Odgaard, T. Asset, P. Atanassov, I. V. Zenyuk, *J Power Sources* **2022**, *551*. https://doi.org/10.1016/j.jpowsour.2022.232209.
[44] A. Kneer, N. Wagner, *J Electrochem Soc* **2019**, *166* (2), F120–F127. https://doi.org/10.1149/2.0641902jes.
[45] A. Kneer, N. Wagner, C. Sadeler, A.-C. Scherzer, D. Gerteisen, *J Electrochem Soc* **2018**, *165* (10), F805–F812. https://doi.org/10.1149/2.0651810jes.
[46] P. Thiele, Y. Yang, S. Dirkes, M. Wick, S. Pischinger, *Int J Hydrogen Energy* **2024**, *52*, 1065–1080. https://doi.org/10.1016/j.ijhydene.2023.08.292.
[47] T. Đukić, L. J. Moriau, I. Klofutar, M. Šala, L. Pavko, F. J. González López, F. Ruiz-Zepeda, A. Pavlišič, M. Hotko, M. Gatalo, N. Hodnik, *ACS Catal* **2024**, *14* (6), 4303–4317. https://doi.org/10.1021/acscatal.3c06251.
[48] R. K. F. Della Bella, B. M. Stühmeier, H. A. Gasteiger, *J Electrochem Soc* **2022**, *169* (4), 044528. https://doi.org/10.1149/1945-7111/ac67b8.

Manuscript received: November 24, 2024
Revised manuscript received: February 2, 2025
Version of record online: ■■, ■■

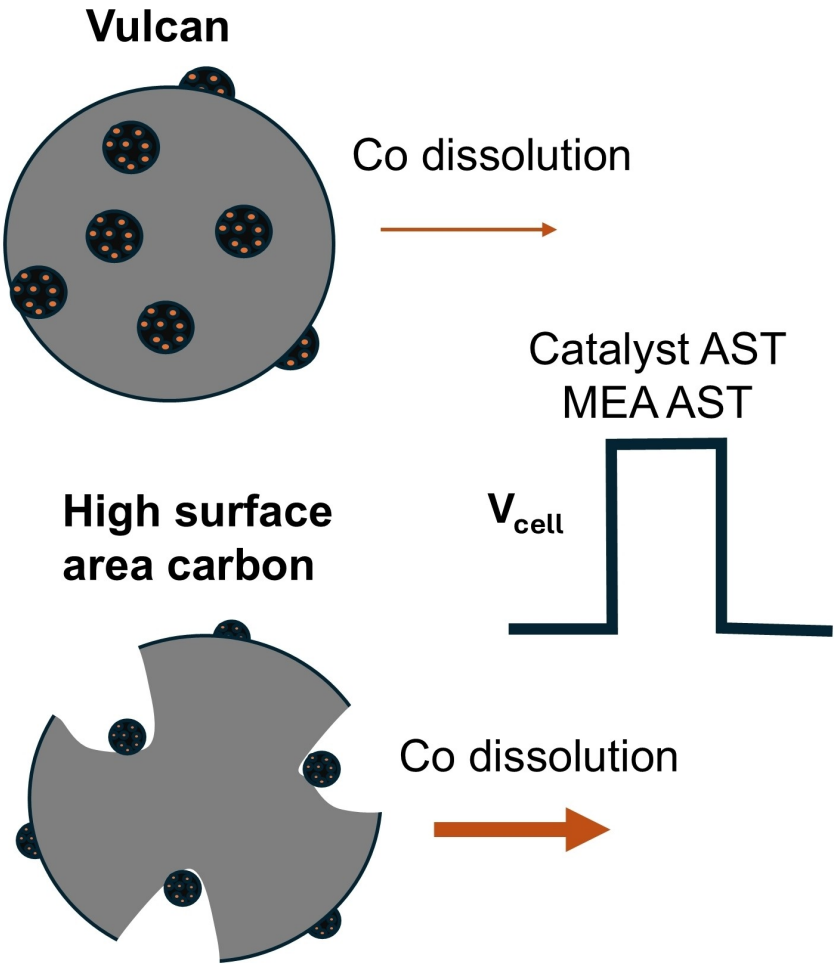

Higher degradation of catalyst observed for PtCo supported on high surface area carbon when subjected to two accelerated stress tests (ASTs) for polymer electrolyte fuel cells.

C. H. Chen, M. Coats, F. Chabot, Y. Morimoto, P. Atanassov, N. Tamura, J. Braaten, B. M. Stühmeier, C. Johnston, S. Pylypenko, L. Cheng*, I. V. Zenyuk**

1 – 17

Durability of Pt-Alloy Catalyst for Heavy-Duty Polymer Electrolyte Fuel Cell Applications under Realistic Conditions